Bayesian inference of neural connectivity in a population of neurons from calcium imaging data

(Dated: July 20, 2009)

We present Bayesian framework for inferring connectivity in a network of coupled neurons, observed simultaneously using calcium imaging.

Contents

I. MOTIVATION

Since Ramon y Cajal discovered that the brain is not a syncytium, but rather a rich and dense *network* of neurons, neuroscientists have wondered about the details of these networks. Since then, while much has been learned about "macro-circuits" — the connectivity between populations of neurons — relatively little is known about "micro-circuits" — the connectivity within populations of neurons. Broadly, one can imagine two distinct strategies for inferring microcircuit connectivity: anatomical and functional.

Anatomical approaches, while perhaps the gold standard for questions of connectivity, are often exceedingly laborious. Historically, neuroanatomists used tracing studies to address these questions, i.e., filled individual neurons with various dyes, and looked where the axons and dendrites terminated [**?**]. Besides being problematic with respect to whether the dyes filled the processes to the far proximal limit, or merely until the diameter became too small [**?**], this process is tedious and very low throughput. Recently, experimentalists have developed fluorescent proteins that express throughout the dendritic tree [**?**] or axonal arborization [**?**], that potentially resolves the premature termination issue, but not the throughput issue. Complementary to these labeling ideas, others have been developing Electron Microscopy based strategies to slice up neural tissue [**?**], and then automate track tracing using sophisticated image processing software [**?**]. This strategy has great promise for improving the throughput of these neuroanatomical studies, but have not yet quite achieved "off-the-shelf" status for experimental neuroscientists. Combining these powerful microscopy/computational tools with the genetic sensors, is perhaps the most promising emerging technology to date, but would still require hundreds to thousands of computational hours to infer the microcircuit for even small populations of neurons, such as part of a retina [**?**].

In contrast to the above described anatomical approaches, there has been relatively little work directed at developing tools for inferring microcircuits using *functional* data.

Emerging ideas, such as combining the power of Brainbow and GRASP [32, 33], may

Our belief is that this dearth of knowledge stems largely from a paucity of tools developed to address questions of microcircuitry. That being said, in the recent decades, several such tools have emerged.

For instance, calcium-sensitive fluorescent indicators provide a glimpse into the spiking activity of neurons, in a relatively non-invasive manner [**?**]. Very recently, some indicators achieve signal-to-noise ratios (SNRs) yielding single spike resolution [**?**]. In combination with these dyes, bulk-loading techniques enable experimentalists to simultaneously fill populations of neurons with such dyes [**?**]. While these approaches are state-of-the-art in terms of SNR, their invasiveness is a significant drawback. To that end, genetically encoded calcium indicators are under rapid development from a number of groups, and they are approaching SNR levels of nearly single spike accuracy as well [**?**]. Regardless of the source of the fluorescence, microscopy technologies for collecting the signal are also rapidly developing. Cooled CCDs for wide-field imaging (either epifluorscence or confocal) now achieve a quantum efficiency of $\approx 90\%$ with frame rates easily exceeding 30 or 60 Hz [**?**]. For in vivo work, 2-photon laser scanning microscopy

Complementary strategies for collecting the fluorescence signals — whether the source be organic dyes or genetic sensors –

Regardless of how the indicators get in the cells,

A complementary approach to obtaining populations of neurons that fluoresce as a function of calcium concentraion

nother approach rapidly progressing is the development of genetically encoded calcium indicators

Our aim here is to contribute a computational tool, that will enable one to infer the connectivity within a population of neurons, given only poor information regarding their activity.

through laborious neuroanatomical studies, the twenty-first century brings with it the possibility utilizing powerful technological advances to create high-throughput tools for asking quantitative neurobiological questions. In particular, our aim here is to develop computational tools that facilitate inferring the functional connectivity between a population of observable neurons, using calcium-sensitive fluorescence sensors.

The problem of reconstructing connectivity in neural circuits in the brain has recently gained much attention [5, 18–21, 50]. In particular, amid growing evidence of the importance of collective effects in neural networks [6, 23, 42], the problem of understanding neural substrates of behavior and cognition via the structure of neural circuits had gradually moved into the spotlight of neuroscience research [2, 8, 9, 12, 17, 46, 51, 52].

Traditionally, one is interested in recovering the structure of neural circuit in the form of a wiring diagram specifying the list of synaptic connections in a particular population of neurons alongside with the synaptic connections' strengths and types. Few different approaches for such comprehensive reconstruction of neural circuits had been proposed in the past including serial section electron microscopy [5, 20], diffusion tensor imaging [18, 19], ensembles of fluorescent tracers [3], and others. Electron microscopy remains the standard for neuroanatomical circuits reconstruction with example of complete nervous system reconstruction in C. *elegans* available in the literature [51, 52]. Electron microscopy, however, is known to be extremely expensive, slow and laborious method - reconstruction of the above mentioned circuit with only 300 neurons and fewer than 10^4 connections took over a decade to complete. Even with recent developments in automated data acquisition [50] and image-processing [22, 24, 31], electron microscopy remains an approach limited by long imaging times and extreme vulnerability to errors in neural tracing and image analysis. Diffusion tensor imaging [19] and ensembles of fluorescent tracers [3] potentially offer a technique capable of much faster reconstructions and much larger circuits (also in live subjects in diffusion tensor imaging). However, low resolution of these techniques limits them to only the highest-level information about neural circuit organization, forgoing the fine details of neural connectivity.

Although recently suggested method for collating information from ensembles of fluorescent markers using Compressive Sensing [32, 33] may allow to overcome both the speed limitation of electron microscopy and resolution limit of optical techniques, this method requires development of novel genetic constructs and may be challenging to scale up to larger circuits. Overall, the problem of large scale reconstructions of the structure of neural circuits using neuroanatomy approach remains extremely challenging endeavor.

Another family of methods for inferring neural connectivity is using observations of neural activity in population of neurons, such as micro-electrodes recordings of external field potential [27–29, 40, 48] or functional magnetic resonance imaging (fMRI) [NEED REF]. Unlike the neuroanatomy approach, these techniques illuminate the structure of neural circuits in terms of their functional connectivity. Functional connectivity may be defined as the statistical effect one neuron's activity has upon another, i.e. two neurons are functionally connected if their spike trains are conditionally dependent given all the other observable variables, including the stimulus and the activity of all other neurons.Although details of the relationship between functional connectivity and anatomical circuit structure are yet to be elaborated, empirical knowledge of functional connectivity is important both fundamentally and for applications. Immediate knowledge of both functional and anatomical connectivity may be required to elucidate the relationship between the two, and also functional connectivity provides access to invaluable information about coding and decoding of signals in neural populations necessary for applications such as neural interfaces or neuro-prosthetics.

Despite their numerous advantages and many applications, both micro-electrode recordings and fMRI have also serious limitations. In case of external field recordings, application of this approach are limited by the size of largest

micro-electrode arrays restricting the largest size of neural population that can be observed. Neural population with only ≤ 100 cells can be simultaneously observed in state of the art experiments. fMRI, although potentially giving fast access to the entire brain in in-vivo conditions, is constrained by bad spatial and temporal resolution of fMRI signal, and uncertain relationship of fMRI signal (i.e. blood flow) with the neural activity.

Recently, great advances in the development of calcium indicators, delivery techniques, and microscopy technologies have facilitated calcium imaging of neural activity of large populations of neurons in a wide array of neural substrates [15, 21, 34, 36]. Calcium imaging is an excellent tool for collecting large-scale data for functional connectivity, and is potentially capable of overcoming both the resolution limits of fMRI and population size limit of multi-electrode arrays. With calcium imaging, recordings at the level of individual cells are possible for thousands and tens of thousands of cells while retaining resolution sufficient for reconstruction of individual spikes [21]. In this paper we develop a Bayesian formalism for inferring neural connectivity in a population of neurons from such calcium imaging data.

II. METHODS

Our goal is to estimate the most likely connection matrix from a population of observable neurons, given only their calcium fluorescence observations. We take a model based approach, meaning that we first describe a parametric generative model that completely characterizes the statistics of the data, and then we derive algorithms to learn the parameters, given the data.

We use the following conventions throughout the paper, unless indicated otherwise. Time is discrete, taking values $t = 1, \ldots, T$. We let $X_i(t)$ indicate the state of neuron i at time t, $X_i = \{X_i(t), t = 1, \ldots, T\}$, and $\mathbf{X} = \{X_1, \ldots, X_N\}$. Conditional probability distributions will be written $P[\mathbf{F}|\mathbf{X}; \theta]$, where $\mathbf{X}$ indicates some random variables, θ indicates some parameters, and a semicolon separates the two. To indicate that a random variable, X, is independently and identically distributed according to some distribution P, we have $X \overset{iid}{\sim} P$.

A. Model

We first describe the model that characterizes the statistics of the joint spike trains of all N observable neurons. Each neuron is modeled as a generalized linear model (GLM), which is known to capture well the statistical properties of the firing of individual neurons [37, 38, 40, 43, 53]. More specifically, we say that at time t, the probability of neuron i spiking is given by some nonlinear function, $f(\cdot)$, of the input to that neuron at that time, $J_i(t)$. The input is composed of: (i) some baseline firing rate, b_i, and (ii) spike history terms, $h_j(t)$, from each neuron j, weighted by ω_{ij}:

$$n_i(t) \overset{iid}{\sim} \text{Bernoulli}\big(f\big(J_i(t)\big)\big), \qquad J_i(t) = b_i + \sum_{j=1}^{N} \omega_{ij} h_j(t), \tag{1}$$

To ensure mathematical tractability, we must impose some constraints on $f(\cdot)$ and the dynamics of $h_j(t)$. More specifically, $f(\cdot)$ must be convex and log-concave, to ensure that the likelihood of the parameters of this model has a single maximum, facilitating efficient computations [38]. In all the below simulations, we let $f(J) = \mathrm{e}^{\mathrm{e}^{-J}\Delta}$, where the inclusion of Δ, the time step size, ensures that the firing rate is independent of the particular time discretization of our model (see [**?**] for a proof that this $f(\cdot)$ satisfies the above constraints). Furthermore, as the algorithms we develop below assume Markovian dynamics, we model the spike history terms as:

$$h_j(t) = (1 - \Delta/\tau_h) h_j(t-1) + n_j(t) + \sigma_h \sqrt{\Delta} \epsilon_j^h(t). \tag{2}$$

where τ_h is the decay time constant for spike history terms, σ_h is the standard deviation of noise, $\sqrt{\Delta}$ ensures that noise statistics are independent of the time discretization, and throughout this paper, $\epsilon_\cdot^\cdot$ is assumed to be an independent standard normal random variable, i.e., $\epsilon_\cdot^\cdot(t) \overset{iid}{\sim} \text{Normal}(0, 1)$. Note that this model generalizes straightforwardly to allow each neuron to have several spike history terms, each with a unique time constant, together imparting a wide variety of possible post-synaptic effects, including bursting, facilitating, and depressing synapses [38]. We assume that τ_h and σ_h are known, and therefore our model spiking parameters $\theta^n = \{\theta_i^n\}_{i=1}^N$, where $\theta_i^n = \{\omega_i, b_i\}$, where $\omega_i = (\omega_{i1}, \ldots, \omega_{iN})$.

The problem of estimating functional connectivity, given a model like the one above, when neural spikes $n_i(t)$ are assumed to be directly observed, has recently received much attention [40]. With calcium imaging, however, we do not directly observe spike trains. Instead, fluorescent signal from the calcium indicators conveys neural activity via hidden nonlinear calcium dynamics [49]:

$$C_i(t) = C_i(t-1) + (C_i^b - C_i(t-1))\Delta/\tau_i^c + A_i n_i(t) + \sigma_i^c\sqrt{\Delta}\epsilon_i^c(t), \tag{3}$$

$$F_i(t) = \alpha_i S(C_i(t)) + \beta_i + \sqrt{\gamma_i S(C_i(t)) + \sigma_i^F}\epsilon_i^F(t). \tag{4}$$

Eq. (3) describes evolution of intracellular calcium concentration $C_i(t)$ in the neuron i at time t. Under normal conditions, $C_i(t)$ fluctuates around the baseline level of C_i^b with normally distributed noise $\epsilon_i^c(t)$ with standard deviation $\sigma_i^c\sqrt{\Delta}$. Whenever the neuron fires a spike, $n_i(t) = 1$, causing the calcium to jump by A_i, and subsequently decay with time constant τ_i^c. The fluorescence signal corresponding to neuron i at time t, $F_i(t)$, corresponds to the count of photons collected at the detector per neuron per imaging frame. It is distributed according to normal statistics with the mean and variance given by generalized Hill functions, where $S(C) = C/(C + K_d)$ [54]. Because K_d effectively scales the results, and is a property of the indicator, we assume throughout this work that it is known. Therefore, each neuron has parameters $\theta_i = \{\omega_{ii}, b_i, C_i^b, \tau_i^c, A_i, \sigma_i^c, \alpha_i, \beta_i, \gamma_i, \sigma_i^F\}$ independent of the other neurons. The ω_{ii}'s make up the diagonal of the functional connection matrix, $\omega = \{\omega_i\}_{i=1}^N$, yielding a total of $|\theta| = (9+N)N$ parameters for our model. Note that collectively Eqs. (1) – (4) defined a coupled hidden Markov model (HMM) [45].

B. Goal and general strategy

Given the above model, our goal is to estimate the functional connectivity matrix, ω, given calcium imaging observations $\mathbf{F}$. A natural choice is find the *maximum a posteriori* (MAP) estimate:

$$\widehat{\omega} = \underset{\omega}{\operatorname{argmax}}\, P[\omega|\mathbf{F}] = \underset{\omega}{\operatorname{argmax}} \iint P[\theta|\mathbf{X},\mathbf{F}]d\mathbf{X}d(\theta\backslash\omega] \tag{5}$$

where $\theta\backslash\omega$ is the set of parameters excluding the functional connectivity matrix. Because directly solving Eq. (5) is intractable, we utilize the Expectation Maximization (EM) framework, in which one recursively updates the expected value of the joint distribution of $(\mathbf{X},\mathbf{F})$ (E step), and then maximizes all the parameters (M step):

$$\textbf{E step: Evaluate } Q(\theta^{(l+1)},\theta^{(l)}) = E_{P[\mathbf{X}|\mathbf{F};\theta^{(l+1)}]}[\ln P[\mathbf{F},\mathbf{X}|\theta^{(l)}]] = \int P[\mathbf{X}|\mathbf{F};\theta^{(l+1)}]\ln P[\mathbf{F},\mathbf{X}|\theta^{(l)}]d\mathbf{X}$$

$$\textbf{M step: Solve } \theta^{(l+1)} = \underset{\theta}{\operatorname{argmax}}\, Q(\theta,\theta^{(l)})$$

Because our model is a coupled HMM, Q simplifies:

$$\begin{aligned} Q(\theta,\theta^{(l)}) = \sum_{\substack{i\in[1,\ldots,N]\\ t\in[1,\ldots,T]}} & P[C_i(t)|F_i;\theta_i]\times\ln P[F_i(t)|C_i(t);\theta_i] \\ & + P[C_i(t),C_i(t-1)|F_i;\theta_i]\times\ln P[C_i(t)|C_i(t-1),n_i(t);\theta_i] \\ & + P[\mathbf{h}(t)|\mathbf{F};\theta]\times\ln P[n_i(t)|\mathbf{h}(t);\theta_i^n], \end{aligned} \tag{6}$$

where $\mathbf{h}(t) = \{h_i(t)\}_{i=1}^N$. Note that while the first two terms in Eq. (6) only require posteriors marginalized over each neuron, and all but nearest time bins, $P[X_i(t),X_i(t-1)|F_i;\theta_i]$, whereas the last term requires the joint posterior over all neurons (but marginalized over time), $P[\mathbf{X}(t)|\mathbf{F};\theta^n]$.

Unfortunately, analytic solutions for all these posteriors are intractable, so we are forced to use approximate methods to estimate them. To estimate $P[X_i(t),X_i(t-1)|F_i;\theta_i]$ — hereafter called "marginal posteriors" — we utilize a forward-backward procedure that discretize the integrals by sampling [1, 11, 13, 25, 30, 35]. These sequential Monte Carlo (SMC) algorithms (or, "particle filters") operate very efficiently, scaling linearly with time [41]. However, as the dimensionality of the hidden state space increases, importance sampling becomes relatively inefficient. For a population of about 50 neurons, the dimensionality of our model would be $3N = 150$ — too large for existing SMC methods [**?**].

To solve this problem, we propose a hybrid Markov Chain Monte Carlo (MCMC) Gibbs sampling strategy taking advantage of the specific structure of the model Eqs. (1) and (2), namely, that it can be viewed as a set of N coupled HMM models. Gibbs sampling is a procedure for obtaining samples from high-dimensional distributions $P[\mathbf{X}]$ by sampling from low-dimensional conditional distributions $P[X_i|\mathbf{X}_{\setminus i}]$ [14]. This sampling procedure reduces intractable high-dimensional sampling problems to sequences of tractable low-dimensional subproblems. Below, we propose to sample in blocks of one spike train at a time, using MCMC to sample entire spike trains.

The maximization step of EM requires maximizing the conditional expectation of $\ln P[\mathbf{X}, \mathbf{F}|\theta]$ given such samples. Although this is a maximization over $(9+N)N$ parameters, the special structure of Eq. (6) allows one to simplify this optimization problem dramatically by performing optimization with respect to each neuron independently.

Our EM algorithm therefore requires solving four problems: (i) estimating marginal posteriors over neurons, $P[X_i(t), X_i(t-1)|F_i; \theta_i]$ using SMC, (ii) updating the parameter estimates by maximizing the conditional expectation of $\ln P[X_i, F_i|\theta_i]$, (iii) estimating the joint posteriors over all neurons, $P[\mathbf{X}|\mathbf{F}; \theta]$ using a Gibbs technique, and (iv) solving for next iteration of parameters θ^n by maximizing conditional expectation of $\ln P[\mathbf{X}, \mathbf{F}|\theta^n]$. Below, we describe each of these steps in detail. Table 1 provides pseudocode for our general approach.

Algorithm 1 Pseudocode for estimating functional connectivity from calcium imaging data using EM. Note that η^n, η^F, N_G are somewhat arbitrarily chosen bounds.

while $|{\theta_i}^{(l)} - {\theta_i}^{(l-1)}| > \eta^n$ **do**
  for all $i = 1 \dots N$ **do**
    while $|{\theta_i}^{(l)} - {\theta_i}^{(l-1)}| > \eta^F$ **do**
      Sample $X_i \sim P[X_i|\mathbf{F}_i; \theta_i]$
      Maximize ${\theta_i}^{(l+1)} = \text{argmax}_{\theta_i} E\left[\ln P[X_i|F_i; \theta_i]\right]$
    end while
  end for
  for $k = 1 \dots N_G$ **do**
    for all $i = 1 \dots N$ **do**
      Sample $X_i \sim P[X_i|\mathbf{X}_{\setminus i}, \mathbf{F}_i; \theta_i^n]$
    end for
  end for
  Maximize $\theta_i^{n\,(l+1)} = \text{argmax}_{\theta_i^n} E\left[\ln P[\mathbf{X}|\mathbf{F}; \theta^n]\right]$
end while

C. Estimating marginal posteriors over independent neurons using SMC, and learning their parameters

As stated above, our goal here is to derive an algorithm to efficient estimate $P[X(t), X(t-1)|F; \theta]$, which we refer to as the marginal posterior over each neuron (but note that it is also marginalized over all but nearest time bins). As this was discussed at length in [49], here we only provide a brief overview. The standard forward-backward equations provide these posteriors, assuming the below integrals can be evaluated:

$$P[X_t|F_{1:t}] = \frac{1}{Z} P[F_t|X_t] \int P[X_t|X_{t-1}] P[X_{t-1}|F_{1:t-1}] dX_{t-1} \tag{7}$$

$$P[X_t, X_{t-1}|F] = P[X_t|F] \frac{P[X_t|X_{t-1}] P[X_{t-1}|F(1), \dots, F_{t-1}]}{\int P[X_t|X_{t-1}] P[X_{t-1}|F_{1:t-1}] dX_{t-1}} \tag{8}$$

where we have dropped the subscript i, replaced (t) with ${}_t$, introduced notation that $X_{1:t} = (X(1), \dots, X(t))$, and dropped the conditioning on the parameters for brevity sake. Because the integral in Eq. (7) cannot be analytically evaluated for our model, we approximate it with a sum using a sequential Monte Carlo (SMC) framework. More specifically, we sample from $x_t \sim P[X_t|X_{t-1}, F_{1:t}]$, and call each sample a "particle". Given an entire particle swarm, we can compute the relative likelihood (or "weight") of each particle:

$$P[x_t|F_{1:t}] = \frac{1}{Z} \frac{P[F_t|x_t] P[x_t|x_{t-1}] P[x_{t-1}|F(1), \dots, F_{t-1}]}{P[x_t|x_{t-1}, F_{1:t}]} \tag{9}$$

where Z is a normalizing constant ensuring that $\sum P[x_t|F_{1:t}] = 1$. Given these weights, we resample to reduce the variance of the particles. Recursing these three steps (sample, compute weights, resample) for $t = 1, \dots, T$ completes

the approximation to Eq. (7). We can now plug these approximations into Eq. (8), to recursively obtain particle approximations to marginal posteriors over neurons, $P[X_t, X_{t-1}|F]$. Trivially, we can sum over X_t to get marginal posteriors of X_{t-1}.

The sufficient statistics for estimating the parameters for each neuron, θ_i, are these very marginal posteriors. As shown in Eq. (6), this maximization problem decouples into separate subproblems. Specifically, the first term depends on only $\{\alpha_i, \beta_i, \gamma_i, \sigma_i\}$, which we can estimate by recursively solving a quadratic problem for $\{\alpha_i, \beta_i\}$ while holding $\{\gamma_i, \sigma_i\}$ fixed, and then holding $\{\alpha_i, \beta_i\}$ fixed, while estimating $\{\gamma_i, \sigma_i\}$. Considering only the second term, we can estimate $\{\tau_i^c, A_i, C_i^b\}$ again using a quadratic solver, and use the residuals to estimate σ_i^c. Note that all the parameters mentioned so far are constrained to be non-negative, but may be solved very efficiently using Matlab's `quadprog`, providing the appropriate constraints (and the gradients and Hessians, if desirable). Finally, the last term, assuming each neuron is independent, may be written:

$$E[\ln P[n_i(t)|\mathbf{h}_i(t)]] = P[n_i(t)|F_i] \ln(1 - \exp\{-\exp\{b_i + \omega_{ii} h_i(t)\}\Delta\}) + (1 - P[n_i(t)|F_i])(-\exp\{b_i + \omega_{ii} h_i(t)\}\Delta)] \quad (10)$$

which is concave in $\{b_i, \omega_{ii}\}$, and may therefore be solved efficiently using any gradient ascent solver. In practice, we've found that imposing constraints on $\{b_i, \omega_{ii}\}$ improves both the robustness and efficiency of estimating these parameters. Our rational is that the double exponential is such a strong nonlinearity, that as the absolute value of these parameters approaches ≈ 10, the likelihood becomes effectively flat. We therefore restrict these parameters to be within $[-5, 15]$, using Matlab's `fmincon`.

Our procedure therefore is to initialize the parameters for each neuron using some default values that we've found to be effective in practice, and then recursively (i) estimate the marginal posteriors (E step), and (ii) maximize the parameters (M step), using the above described approach. We iterate these two steps until the change in parameters does not exceed some minimum threshold, η^n. We can then use the marginal posteriors from the last iteration to seed our Gibbs sampling procedure described below, to obtain an estimate of $P[\mathbf{h}(t)|\mathbf{F}]$.

D. Estimating joint posteriors over weakly coupled neurons

Computing the most likely estimates of the functional connectivity matrix, ω, requires maximizing the third term of Eq. (6), with respect to $\omega = \{w_{ij}\}$, which can be expanded:

$$E[\ln P[n_i(t)|\mathbf{h}_i(t)]] = P[n_i(t)|F_i] \ln(1 - \exp\{-\exp\{b_i + \sum_j \omega_{ij} h_j(t)\}\Delta\}) + (1 - P[n_i(t)|F_i])(-\exp\{b_i + \sum_j \omega_{ij} h_j(t)\}\Delta)]. \quad (11)$$

This requires having the joint posterior, $P[\mathbf{X}|\mathbf{F}; \theta^n]$, over *all* neurons. However, the algorithm described in Section II C merely provides the marginals over each neuron, $P[X_i(t)|F_i; \theta_i]$. Therefore, in this section, we describe two approaches to infer the joint posteriors: one that makes an independence assumption, and one that is exact.

1. *Independent assumption for approximating the joint posteriors*

If the SNR in the calcium imaging is high, the fluorescence data of each neuron provides nearly all the information about spike times. Thus, the joint posterior approximately factorizes into a product of the marginal posteriors for each neuron:

$$P[\mathbf{h}(t)|\mathbf{F}; \theta] \approx \prod_{i=1}^{N} P[h_i(t)|F_i; \theta_i]. \quad (12)$$

Given this approximate joint posterior, we use these approximately sufficient statistics to estimate the functional connection matrix, ω. When this approximation is accurate, we obtain a considerable speed-up in processing, not just because it obviates the need to generate joint samples, but also because we can parallelize the algorithm, inferring

the marginals for each neuron on a separate processor. This will be required for estimating the functional connection matrix online, as will be discussed more in Section IV.

We refer to such procedure for estimating the joint posterior as the independent approximation. Depending on the accuracy of such approximation, it may or may not be acceptable for the estimation of the true functional connectivity matrix ω. However, as we show below, it is indeed the case that the independent approximation is adequate here for calcium imaging with reasonable SNR.

2. An exact sampling procedure to estimate the joint posteriors

As mentioned above, the sufficient statistic for computing the maximum likelihood estimate of the functional connection matrix, ω, is the joint posterior, $P[\mathbf{X}(t)|\mathbf{F};\theta^n]$. Unfortunately, the SMC approach described in Section **??** does not scale well as the number of hidden states increases. Therefore, our aim in this section is to develop an algorithm that builds on top of the SMC approach, that yields the sufficient statistics of interest. A relative naive approach would be to use a vanilla Gibbs sampler to approximate the joint posteriors, of the form:

$$X_i(t) \sim P[X_i(t)|\mathbf{X}_{\setminus i}, X_i(1), \ldots, X_i(t-1), X_i(t+1), \ldots, X_i(T), \mathbf{F}; \theta^n]. \tag{13}$$

Unfortunately, this approach is likely to mix very poorly, due to the strong temporal dependence between $X_i(t)$ and $X_i(t+1)$, for all t. Instead, we propose to use a block-Gibbs strategy, sampling each spike train as a block:

$$X_i \sim P[X_i|\mathbf{X}_{\setminus i}, \mathbf{F}; \theta^n]. \tag{14}$$

which is likely to mix quickly, given that spike trains are only weakly coupled. The SMC methods described above, however, yield only marginals over time, $P[X_i(t), X_i(t+1)|\mathbf{F};\theta]$, and are therefore insufficient. We could sample the spike train from the set of particle swarms generated above (using a variant of finite forward-backward procedure, related to the Viterbi procedure [41]). Such procedure, however, is known to result in biased samples [1, 35]. Specifically, such samples are distributed with the probability density

$$X_i \sim \frac{1}{Z(G)} P[X_i(t=1)|\omega] \prod_{t=2}^{T} P[X_i(t)|X_i(t-1);\omega] \prod_{t=1}^{T} P[F_i(t)|X_i(t);\theta_i] \tag{15}$$

$$Z(G) = \sum_{\{X_i(t)\}\in G} P[X_i(t=1)|\omega] \prod_{t=2}^{T-1} P[X_i(t)|X_i(t-1);\omega] \prod_{t=1}^{T} P[F_i(t)|X_i(t);\theta_i]. \tag{16}$$

where $G = \prod_t G(t)$ is the collection of particle swarm samples $G(t) = \{X_i^{(l)}(t) : X_i^{(l)}(t) \sim P[X_i(t)|\{\mathbf{F}_i;\theta_i]$. In particular, such probabilities of different sequences differ from the true probabilities by the difference in the estimated normalization constant $Z(G)$ from the true normalization Z. This bias may be removed by embedding SMC into a larger importance sampling algorithm, correcting for bias $Z(G)$ by retaining SMC samples with probability $\sim Z(G)$ [1]. In particular, Andrieu et al. [1] show that as the size of the particle swarm grows the acceptance ratio of such importance sampling tends to unity.

A different approach, developed by Neal et al. [35], is to use Markov Chain Monte Carlo method (MCMC) with the Markov chain constructed specifically to have the necessary equilibrium distribution $P[\mathbf{X}|\mathbf{F};\theta]$. The Markov Chain is constructed as follows. First, continuous-state HMM is replaced with a discrete HMM on the grid, $G = \prod G(t)$. At each time-point t, we therefore define a pool of L grid-points $\{X_i^{(l)}(t)\}$ drawn independently from a given proposal density $\rho_i^t[X_i(t)]$. The grid G is then constructed as a direct product of such pools. Second, sequence of states is selected over such grid with the probability

$$X_i \sim P[X_i(t=1)|\mathbf{X}_{\setminus i};\theta_i] \prod_{t=2}^{T} P[X_i(t)|X_i(t-1), \mathbf{X}_{\setminus i};\theta_i] \prod_{t=1}^{T} \frac{P[F_i(t)|X_i(t);\theta_i)}{\rho_i^t[X_i(t)]}. \tag{17}$$

This may be done directly and efficiently using forward-backward procedure with the observation probability modified to $P[F_i(t)|X_i(t),\theta_i] \to P[F_i(t)|X_i(t),\theta_i)/\rho_i^t[X_i(t)]$. XXX Y: i'm not sure what you mean here. XXX

Finally, states from the chosen sequence of states X_i should be included in the pools $G(t)$ for the next MCMC step, $X_i(t) \in G(t)$, and the above two steps should be repeated with the new grid G. It is shown in [35] that the limiting distribution of such Markov chain is the correct unbiased distribution

$$X_i \sim P[X_i(t=1)|\mathbf{X}_{\setminus i};\theta_i] \prod_{t=1}^{T-1} P[X_i(t)|X_i(t-1),\mathbf{X}_{\setminus i};\theta_i] \prod_{t=1}^{T} P[F_i(t)|X_i(t);\theta_i]. \tag{18}$$

The advantage of Neal's method (over embedding SMC into an importance sampler) are that (i) the grids G are simple to prepare, and (ii) no importance sampling rejection step is required, as such a step is implicitly accommodated in the forward-backward procedure via modified observation probability Eq. (17).

The proposal density, $\rho_i^t[X_i(t)]$, may be chosen arbitrary as long as it has sufficiently large support. To achieve faster convergence, we use marginal densities $P[X_i(t)|\mathbf{X}_{\setminus i},\mathbf{F};\theta_\mathbf{i}]$ computed from the conventional SMC algorithm. Such an efficient proposal density allows the Markov Chain to converge extremely quickly. More specifically, we let $\rho_i^t[X_i(t)] = \rho_t^i[C_i(t)]\rho_t^i[n_i(t)]\rho_t^i[h_i(t)]$. The proposals for calcium, $\rho_t^i[C_i(t)]$, were mixtures of Gaussians centered on particles from the particle swarm $C_i^{(l)}(t)$ with the variances $\approx var\left[C_i^{(l)}(t) - C_i^{(l')}(t)\right]$. $\rho_t^i[n_i(t)]$ was taken to be Bernoulli distribution with the spike probability estimated from the particle swarm. Finally, $\rho_i^t[h_i(t)]$ XXX ? XXX. Such samples for single neurons from the conditional probability distributions $P[X_i|\mathbf{X}_{\setminus i},\mathbf{F};\theta]$ may be subsequently used in block-Gibbs sampling procedure to acquire joint sample from $P[\mathbf{X}|\mathbf{F};\theta]$. We repeat the MCMC procedure to sample blocks of one neuron state-sequence at a time $X_i \sim P[X_i|\mathbf{X}_{\setminus i},\mathbf{F};\theta_i]$, sequentially for all neurons $i = 1 \ldots N$ for N_G Gibbs cycles (in practice, we typically take $N_G \approx 10$).

E. Estimating the functional connectivity matrix

In order to perform maximization step of EM, the expectation of the log-likehood Eq. (6) needs to be maximized with respect to $\theta^F = \{\theta_i^F\}$ and $\theta^n = \{\theta_i^n\} = (\omega_i, b_i)$. For N neurons this is a very large optimization problem with $6N$ parameters M and $mN^2 + N$ parameters W. Fortunately, this optimization problem admits dramatic simplifications making it tractable for existing computers. Specifically, estimation of parameters M_i may be performed individually for each neuron since calcium dynamics of different neurons are independent from each other and, given H, also decoupled from GLM. Finding parameters M_i, thus, only involves solving of N 6D-optimization subproblems (see [49] for details).

Finding GLM parameters is an optimization problem with $mN^2 + N$ variables. By construction, however, GLM log-likelihood $P_\mathbf{n}(H, W)$ is convex and, also, GLM log-likelihoods for different neurons, Eq. (**??**), are independent and may be maximized separately. Finding parameters $\{\omega_{ij}(t), b_i\}$, thus, only involves solving of N $mN + 1$-dimensional convex optimization subproblems, which can be done efficiently using standard algorithm such as gradient ascent, conjugate gradient or Newton-Rapson methods. E.g., we used standard Matlab's nonlinear optimization function `fmincon`, provided in optimization toolbox, to solve this problem for up to $N = 500$ neurons.

Simple properties of the connectivity matrix, that may be known a priori, may be extremely helpful in obtaining accurate solutions for smaller datasets. In particular, enforcing sparseness for signal recovered with a series of linear measurements via $L1$-regularizer is known to dramatically reduce the amount of data necessary to accurately reconstruct the signal [7, 10, 33]. Although here the estimation problem is not linear, it is interesting what impact analogous prior might have on the reconstruction of the matrix of functional connection weights W. Enforcing sparseness may be done by introducing exponential prior to GLM [47], thus leading to the posterior probability for the spike train

$$E[\ln P_\mathbf{n}(n_i|\mathbf{n}_{\setminus i}, W)P[W]] = \sum_t E\left(n_i(t)J_i(t) - (1-n_i(t))\exp(J_i(t))\Delta\right) - \lambda \sum_{t'ij} |\omega_{ij}(t')|. \tag{19}$$

Exponential prior parameter $\lambda \sim 1/\langle|\omega_{ij}|\rangle$ may be set from a priori neuroanatomical or neurophysiological data. Sparse prior does not change the convexity of GLM log-likelihood and, so, such regularized problem may be solved efficiently using methods of convex optimization theory. E.g., by introducing slack variables $s_{ij}(t) > |\omega_{ij}(t)|$, this problem may be converted to a nonlinear program that can be solved using interior point method

$$\begin{aligned} &\min\left\{-\sum_t E\left[n_i(t)J_i(t) - (1-n_i(t))\exp(J_i(t))\Delta\right] + \lambda\sum_{t'j} s_{ij}(t')\right\}, \text{ s.t.} \\ &\omega_{ij}(t') < s_{ij}(t'),\ -\omega_{ij}(t') < s_{ij}(t')\ \forall j, t'. \end{aligned} \tag{20}$$

We used Matlab's standard function fconmin, provided in optimization toolbox, to solve this constrained optimization problem for up to $N = 500$ neurons. As we will see below, sparse prior dramatically decreases the amount of data necessary for accurate estimation of the connectivity matrix.

Another property of the connectivity matrix that may be useful is the so called Dale's law. Dale's law is the empirical observation that neurons always make synapses of one kind, i.e. either inhibitory or excitatory. In terms of the connectivity matrix, Dale's law translates into the condition of sign-constancy of the matrix columns. Dale's law is easy to enforce by constraining ω_{ij} to be either positive or negative for given j. Sign assignments may be chosen by inspecting unconstrained solution W and choosing the row $\omega_{i\cdot}$ to be excitatory if the sum-squares of the positive terms ω_{ij} for given j in the unconstrained solution is greater than that of the negative terms, and inhibitory otherwise. After that, Dale's law may be enforced either independently or together with the sparse prior. The nonlinear program in the latter case becomes

$$\begin{array}{l}\min\left\{-\sum_t E\left[n_i(t)J_i(t)-(1-n_i(t)\exp(J_i(t))\Delta\right]+\lambda\sum_{t'j}s_{ij}(t')\right\},\ \text{s.t.}\\ \omega_{ij}(t')<0,\ -\omega_{ij}(t')<s_{ij}(t')\ \forall j,t' \text{ where } j \text{ is inhibitory neuron,}\\ \omega_{ij}(t')<s_{ij}(t'),\ -\omega_{ij}(t')<0\ \forall j,t' \text{ where } j \text{ is excitatory neuron.}\end{array} \tag{21}$$

This optimization problem is essentially equivalent to the constrained optimization problem Eq. (20), and can be solved using the same methods. We used the same Matlab's function `fconmin` to solve this problem. Unlike sparse prior, Dale's prior did not lead to substantial improvement in the reconstructed connectivity matrix.

F. Specific implementation notes

In specific implementation of the above EM algorithm, we break the inference problem into three steps (see algorithm 1). First, we estimate for each neuron i the model of its calcium dynamics M_i, given observations F_i and the currents $J_i(t) = b_i + \sum_j \sum_{t'<t} \omega_{ij}(t-t')n_j(t')$ from the previous EM estimate of $\omega_{ij}(t)$, b_i and $n_j(t)$ (at first iteration $\omega_{ij}(t) \equiv 0$), on a subset of data with $\sim 10-100$ spikes. It is advantageous to perform estimation of M_i separately because this problem may be solved using smaller amount of data ($\sim 10-100$ spikes). Since estimation of W requires processing very large amounts of data ($\sim 1000-3000$ spikes), pre-estimating M_i allows to arrive quicker at a better estimate of W at a lower computational cost. Second, using thus produced calcium dynamics models M_i, we obtained a joint sample of spike-histories $\{n_i(t)\}$ using hybrid MCMC-Gibbs or SMC method above. In this work we accounted for the impact of interactions with other neurons via injected currents $J_i(t)$, which thus accounted for the information about the past neural activity in the population only - $n_i(t) \sim P[n_i(t)|\mathbf{n}(t'), t' = 1 \dots t-1]$. In principle, better samples could be obtained by taking into account spiking of the other neurons at $t' > t$, i.e. sampling from $P[n_i(t)|\mathbf{n}(t'), t' = 1 \dots T]$ [39]. Such improved sampling procedure is a subject of future effort. Reduced history variables $\{h_i(t)\}$ were also computed at the time of obtaining spike samples. Third, given joint spike train samples $\{n_i(t)\}$ or samples of reduced history variables $\{h_i(t)\}$, we performed estimation of the functional connectivity matrix W by solving large convex optimization problem. Steps one through three were then repeated until convergence in the functional connectivity weights W was observed.

Important feature of the above algorithm is that the above procedures straightforwardly parallelize. Estimation of models M_i could be done independently for all neurons. Calculation of the functional connectivity matrix W also involved solving N optimization subproblems for different neurons that could be done independently. In independent approximation, sample $\{n_i(t)\}$ could be obtained in parallel for different neurons; while for hybrid MCMC-Gibbs method obtaining the sample could be parallelized by drawing HMM state-sequences within Gibbs loop for a few neurons at a time, instead of single neuron at a time. High parallelizability of these steps resulted in significant time savings when analysis of calcium imaging data was performed on multi-processor computer or using a super-computing facility. We performed bulk of the calculations on a high-performance cluster of Intel Xeon L5430 based computers (2.66 GHz). For 10 minutes of simulated fluorescence data, calculations typically took 10-20 minutes per neuron using independent approximation, with time split approximately equally between calcium model estimation and obtaining spike-history samples (5-10 min) and solving GLM problem (5-10 min). Hybrid MCMC-Gibbs sampler was substantially slower, up to an hour per neuron per Gibbs pass, with Gibbs sampler being the most computationally expensive part. Parallel computation made calculations for large populations of neurons $N \sim 200-500$ possible.

G. Accuracy of the estimates and Fisher information matrix

In order to determine the necessary amount of data for accurate estimation of the functional connectivity matrix, we calculate Fisher information for $P[W|\mathbf{n}]$. Assuming for simplicity perfect knowledge of spike trains (i.e. such not corrupted by inference errors from calcium imaging) and single time-bin coupling $m = 1$, i.e. $\omega_{ij}[t] \neq 0$ only for time-delay $t = 1$, we write the Fisher information matrix as

$$\begin{aligned} C^{-1} = \frac{\partial(-\ln P)}{\partial\omega_{ij}\partial\omega_{i'j'}} = - \ \delta_{ii'} \sum_t \Big[& n_i(t) n_j(t-1) n_{j'}(t-1) \left(-\frac{f'(J_i(t))^2}{f(J_i(t))^2} + \frac{f''(J_i(t))}{f(J_i(t))} \right) \\ & -\Delta(1-n_i(t)) n_j(t-1) n_{j'}(t-1) f''(J_i(t)) \Big] . \end{aligned} \tag{22}$$

For exponential transfer function $f(J)$ and assuming weak coupling between spikes this may be rewritten as

$$\begin{aligned} C^{-1} \ &= \delta_{ii'}(T\Delta) P[n_i(t)=0, n_j(t-1)=1, n_{j'}(t-1)=1] E[f(J_i(t))|n_i(t)=0, n_j(t-1)=1, n_{j'}(t-1)=1] \\ &\sim (T\Delta) \left[(r\tau_w)\delta_{ii'}\delta_{jj'} + O((r\tau_w)^2) \right] r. \end{aligned} \tag{23}$$

Here $(T\Delta)$ is the total observation time, τ_w is "the coincidence time" - the typical EPSP/IPSP time-scale over which the spike of one neuron affects the spike probability of the other neuron, and $r \approx E[f(J_i(t))|n_i(t) = 0, n_j(t-1) = 1, n_{j'}(t-1) = 1]$ is the typical firing rate. For successful determination of the functional connectivity weights W, the variance C should be smaller than the typical scale $\langle W^2 \rangle$, i.e.

$$(T\Delta) \sim (W^2 r^2 \tau_w)^{-1}. \tag{24}$$

For typical values of $W^2 \approx 0.1$, $r \approx 5$ Hzand $\tau_w \approx 10$ ms, with this order of magnitude estimate we obtain T of the order of hundred seconds. This theoretical estimate of the necessary amount of fluorescent data is in good agreement with our simulations below.

Note also that necessary recording time does not depend on the number of neurons in the imaged network N. This, at first, unexpected result is the direct consequence of the special form of C^{-1} in Eq. (23). In particular, when $r\tau_w << 1$, this matrix is dominated by the diagonal term $(T\Delta)(r^2\tau_w)$, and so the Fisher information matrix is predominantly diagonal with the scale $(r^2\tau_w T\Delta)^{-1}$, independent of the number of neurons N. This theoretical result is also directly confirmed in our simulations below.

III. RESULTS

A. Simulating neural activity in a neural population

To test the described method for inferring functional connectivity from calcium imaging data, we simulated a network of stochastically connected neurons constructed as close as possible to resemble the real cortical microcircuits, based on experimental data available from the literature [4, 16, 26, 44]. We prepared sparse random networks of $N = 10 - 500$ neurons. Each neuron was modeled using Eqs. (1) and (2).

The network was divided into excitatory (80%) and inhibitory (20%) neurons [4, 16], each respecting Dale's law, i.e., all axons for a particular neuron were either excitatory or inhibitory (corresponding to all positive or all negative columns in our functional connection weight matrix, ω). Neurons were randomly connected to each other with probability 0.1 [4, 26] XXX this isn't strictly true, is it? XXX. Synaptic weights for excitatory connections, as defined by EPSP peak amplitude, were randomly drawn from exponential distribution with the mean of $0.5\mu V$ [26, 44]. These were then converted to GLM weights: while synaptic weights physiologically were measured in μV, in GLM functional connectivity weights were measured in log-rate units of Eq. (1)). GLM weights described the change in the probability of the neuron i to fire given neuron j had fired before, as opposed to physiologically measured injected currents or changes in membrane potential. By utilizing this definition, synaptic weights were converted into GLM weights assuming that each EPSP corresponded to added probability of neuron spiking in given time bin of $\Delta P = V_E/V_b$, where v_E is peak EPSP amplitude and V_b is the membrane resting potential below threshold (implying that V_b/V_E EPSPs would be required to trigger neuron over the threshold),

$$\omega_{ij} = \ln(-\ln(e^{-r_i\tau_w} - V_E/V_b)/r_i\tau_w), \tag{25}$$

where $r_i = \exp(b_i)$ is the base firing rate of neuron i and $\tau_w = 10$ msec was the typical EPSP/IPSP scale over which single EPSP affects the firing probability of the neuron i.

Inhibitory connections were also drawn from exponential distribution with the negative mean. Inhibitory connections strength was chosen so as to balance excitatory and inhibitory currents in the network and achieve an average firing rate of ≈ 5 Hz. Practically, the mean strength of inhibitory connections was about 10 times larger than that of the excitatory connections.

The time course of functional connectivity weights $\omega_{ij}(t)$ was modeled as the difference of two exponentials with the rise time of 1 msec and decay time of 10 msec for excitatory and 20 msec for inhibitory currents [44]. Up to 25% variation in these time constants could be allowed. We neglected conduction delays, given that the time delay below ~ 1 msec expected in local cortical circuit was smaller than the time step of our computer simulation. Additionally to excitatory and inhibitory currents, each neuron was modeled to have refractory current with the time-course described as an exponential with time constant of 10 ms.

Spike-trains were generated using GLM by simulating network forward in time with the time step of 1 ms. Given the spike rasters, the fluorescence observations were generated using calcium dynamics model Eq. (3). Parameters for the model were chosen according to our experience with few actual cells analyzed using algorithm of [49], see Table I. The population of cells was generated with these parameters allowing cell-to-cell variance of at least 30%. XXX explain in more detail the distribution from which all the parameters were taken, something like a uniform distribution with bounds based on data. add to table below the bounds too. photon budget should be in terms of the actual parameters of our model XXX Fluorescence was obtained for calcium imaging at the frame-rate of 33 Hzor 66Hz. From 300 sec to 3600 sec of calcium imaging data was simulated.

TABLE I: Table of simulation parameters.

Total neurons	10-500
Excitatory neurons	80%
Connections sparseness	10%
Baseline firing rate	5 Hz
Mean EPSP strength	0.5 μV
Mean IPSP strength	2.3 μV
EPSP profile	1 msec rise time, 10 msec decay time
IPSP profile	1 msec rise, 20 msec decay time
Mean Ca noise σ_c	28 μM
Mean Ca jump A_c	80 μM
Mean Ca background C_b	24 μM
Mean Ca decay time τ_c	0.25 sec
Mean photon budget α_c	1-80 Kph/neuron/frame
K_d	200 μM

B. Inference of the functional connectivity from the simulated calcium imaging data

Connectivity matrix was calculated by solving maximum likelihood problem Eq. (**??**). Specifically,

$$E[\ln P_{\mathbf{n}}(n_i|\mathbf{n}_{\setminus i}; W)] = \sum_t \left(n_i(t) \ln J_i(t) - (1 - n_i(t)) \exp(J_i(t))\Delta\right), \tag{26}$$

$$J_i(t) = b_i + \sum_j \sum_{t'<t} \omega_{ij}(t - t') n_j(t') = b_i + \sum_j w_s^{ij} \sum_{t'<t} \exp(-(t - t')/\tau_h) n_j(t'). \tag{27}$$

The sum in Eqs.(26) and (27) was over the sample of $\{n_i(t)\}$ and over the time-bins t' discretized at the time steps Δ corresponding to the calcium imaging frame rates of either 33 Hz (30 ms) or 66 Hz (15 ms). The coincident time bin $t = t'$ was not used in Eqs.(26)), (27)), i.e. all spike pairs within same time-frame were removed from the GLM fit. Because time position of spikes inferred from fluorescence data typically had inaccuracy $\sim \Delta$, temporal order of such closely positioned spike pairs could be confused in the sample $\mathbf{n}$, thus, polluting GLM dataset. E.g., given two neurons i and j, if the number of spikes of neuron i following neuron j within Δ was m_{ij}, while such in the reverse order was m_{ji}, the difference $\Delta m = m_{ij} - m_{ji}$ effectively corresponded to the difference in GLM weights $\omega_{ij} - \omega_{ji}$. However, if

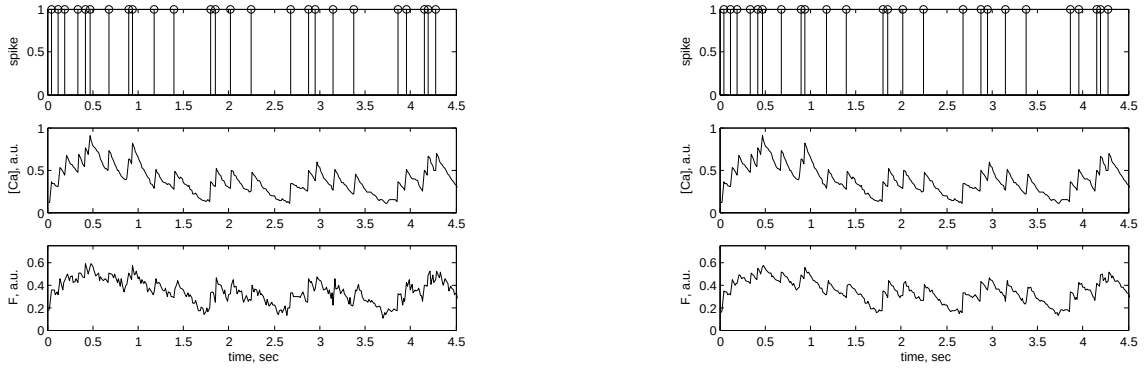

FIG. 1: Examples of calcium and fluorescence traces for low (photon budget 5 Kph/neuron/frame, left) and high SNR regimes (photon budget 40 Kph/neuron/frame, right).

during spike inference the order of such spikes was confused with probability $p \approx 1/2$, the observed number of spike pairs ij would become $m_{ij}(1-p) + m_{ji}p$, while for the reverse order this would be $m_{ji}(1-p) + m_{ij}p$. The difference would thus drop to $\Delta m' = (1-2p)\Delta m$ with the variance remaining the same. This effect complicated the problem of estimating functional connectivity W by effectively mixing ω_{ij} and ω_{ji} and introducing large error in W estimate moving it toward the symmetrized version of W.

Since the connectivity weights $\omega_{ij}(t)$ were time-dependent, to compare inferred and true connectivity we introduced a "scalar" version of the connectivity matrix defined via the peak values of EPSP/IPSP at each connection, i.e. the scalar connection weights were $w_s^{ij} = \mathrm{sign}(\omega_{ij}) \max_t |\omega_{ij}(t)|$. If the time dependence of $\omega_{ij}(t)$ was assumed to be unknown, the first equation in (27)) was used to correlate $n_i(t)$ with $n_j(t')$ for $t' < t$ up to given depth m. Since each next term in Eq. (27)) was exponentially smaller than the previous one, we found that the best results were obtained assuming $m = 1$, allowing for better results by reducing the number of unknowns for the same amount of data. For independent approximation below the time-dependence of $\omega_{ij}(t)$ was assumed to be ''known" exponential, and the weights were estimated using reduced histories $h_i(t) = \sum_{t'<t} \exp(-(t-t')/\tau_h) n_i(t')$ with time constant $\tau_h = 10$ ms. The scalar connection weights were directly estimated as $w_s^{ij} = \omega_{ij}(t=0)$. Such inferred connectivity weights were then compared with true w_s^{ij}.

We shall note that because of coarse time discretization $\Delta \approx 15 - 30$ msec relative to EPSP/IPSP time scale of $\tau_w = 10 - 20$ ms, the first term in the sum (27)) measured in GLM was $\omega_{ij}(\Delta) \approx w_s^{ij} \exp(-\Delta/\tau_w)$, substantially smaller than w_s^{ij}. Time discretization thus resulted in estimated weights differing from the true connectivity by a factor of $\sim \langle \exp(-\Delta/\tau_w) \rangle$, where the average is understood over the spike pairs within two consecutive time-bins. In our simulations, we observed that this factor was a constant for same Δ and τ_w and different network sizes N. For $\Delta = 15$ msec and $\tau_w \approx 10$ msec this factor was ≈ 0.45. Note that where τ_w varied from neuron to neuron, this scaling

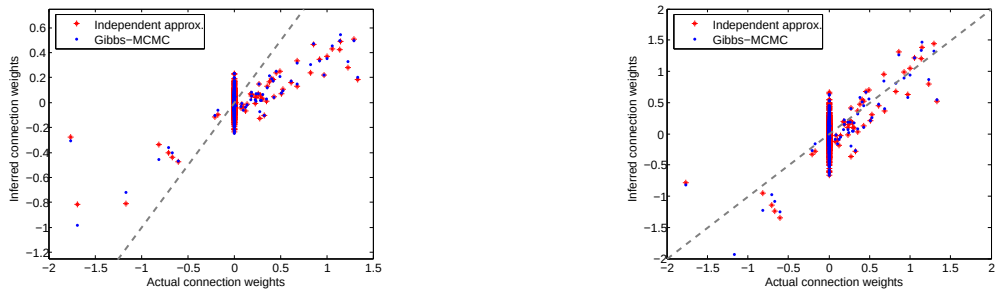

FIG. 2: A scatter plot of inferred connectivity weights vs. real connectivity weights using hybrid MCMC-Gibbs sampler and independent approximation, for a network of $N = 25$ neurons imaged with intermediate SNR (10 Kph/neuron/frame, see Figure 5 below); $r^2 = 0.48$ for MCMC-Gibbs and $r^2 = 0.47$ for IID. Note that the connectivity weights thus inferred are nearly equal, thus showing that independent approximation is sufficient here for the purposes of estimating the connectivity matrix. Note also constant time-discretization scaling bias in the estimated weights due to missing proximal spike pairs (left panel). Scaling-bias adjusted weights correspond to true connectivity weights well (right panel).

factor as well as any mismatch in the time-scale τ_h of $h_i(t)$ and the true EPSP/IPSP time constant τ_w introduced added variability in the estimated weights w_s^{ij}. However, we found such added variance in the estimates of w_s^{ij} to be insignificant for simulations where τ_w was allowed to vary for up to 25% (data not shown).

Scaling bias theoretically could be removed by performing estimation of spike trains with finely discretized time. However, we were not successful in performing this calculation as the amount of data necessary to overcome variation in W introduced by disordering of closely spaced spike-pairs appeared to be well over ≈ 10 min of data used for most of the calculations here. Such high-time-resolution samples of spike trains were also substantially more computationally expensive to obtain and work with. For these reasons we did not pursue this path further, although it may be of interest in the future.

After performing functional connectivity reconstruction using MCMC-Gibbs method, we repeated the reconstruction using independent approximation. We found that MCMC-Gibbs method did not provide noticeable improvement over the independent approximation for imaging regimes where sufficiently accurate connectivity matrix could be recovered, Figure 2. We therefore concluded that the independent approximation was equivalent to exact MCMC-Gibbs method for the purpose of inferring connectivity from calcium imaging data for experimentally interesting regimes.

Since fluorescence data is generally acquired at low frame-rate, one of the main limitation for the connectivity inference from calcium imaging is time-resolution of the inferred spike trains. In order to determine the limits on reconstruction due to this constraint, we compared weights inferred from fluorescence data with such computed from the true spike trains down-sampled at frame-rate of 33 Hz or 66Hz. This served as a baseline for the "best" connectivity matrix reconstructions. We observed that baseline performance could be achieved from calcium imaging data, Figure 3. Also, the same analysis of baseline performance showed that calcium imaging rates below 30 Hz are generally insufficient for the purpose of inferring connectivity, Figure XXX.

[ANOTHER FIGURE 30Hz]

We then considered the question what calcium imaging SNR was required to achieve time-resolution performance limits, particularly as determined by the photon budget of the experimental setup. Photon budget is defined here as the

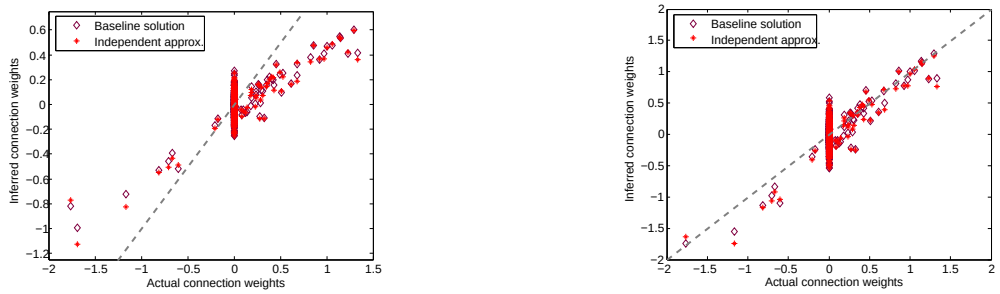

FIG. 3: A scatter plot of inferred connectivity weights vs. real connectivity weights using independent approximation and true spike trains down-sampled to the frame-rate, for a network of $N = 25$ neurons imaged with high SNR (40 Kph/neuron/frame, see Figure 5 below); $r^2 = 0.57$ for IID and $r^2 = 0.57$ for the baseline. Note that for sufficient SNR, the connectivity weights inferred from fluorescence data are nearly equal to such inferred from down-sampled true spikes, thus showing that calcium imaging is capable of achieving accuracy of spike extraction equivalent to direct observation of spike trains. Left panel is the original GLM solution with scaling-bias, and right panel is scaling-bias adjusted solution.

average count of photons collected by the detector from single neuron per single frame. It is experimentally determined by the factors such as dye quantum efficiency, excitation laser power, detector efficiency, microscope scanning speed, etc. Photon budget was one of the primary factors determining possibility of analyzing spike trains from calcium imaging data (the other key factors being frame-rate and neuron peak spike rate). As should be expected, when amount of noise was high (low photon budget), inference from calcium imaging data was far below the baseline level, and with increasing SNR the baseline level was recovered. The SNR level necessary to achieve baseline performance was 20-40 Kph/neuron/frame, Figure 5. For comparison, from our experience with the analysis of real cells [49], the photon budget in real data was ~ 10 Kph/cell/frame for in-vivo data collected at 15 Hz and ~ 100 Kph/cell/frame for in-vitro data at the same frame-rate.

In all cases we found that taking into account sparseness prior resulted in dramatic improvement in the inferred connectivity matrix, allowing to achieve for $T \sim 10$ min the same level of accuracy that would otherwise require over $T \sim 1$ hour of calcium imaging data (Figure 4 and 8). We also explored impact of the Dale's prior and found that improvement in the inferred weights there were much less significant, on the order of 10% in the correlation coefficient r^2. If sparseness of the solution was previously accounted for, accounting for Dale's law led to no improvement in the result (Figure 8).

We finally explored the question how much data was required for given reconstruction accuracy. First, we considered different observation times T, see Figure 8. The observation time necessary to achieve r^2=0.5 was $T \sim 10$ minutes, while with GLM solver using sparse prior $r^2 > 0.6$ was achieved already at $T \sim 5$ minutes of calcium imaging. In agreement with the theoretical analysis of the Fisher information matrix in the Methods, the accuracy of the reconstruction did not depend on the size of the neural network inferred, see Figure 9. Good reconstructions for $N = 20 - 200$ could be obtained in all cases with $T \sim 10 - 30$ min of data. We conclude therefore that the connectivity could be successfully inferred from calcium imaging data, Figures 4, 6 and 8).

"Anatomical" connectivity could be recovered despite potential problems such as common input from correlated neurons, etc. This is owing to the particular form of the activity in our neural network, whereas firing of neurons

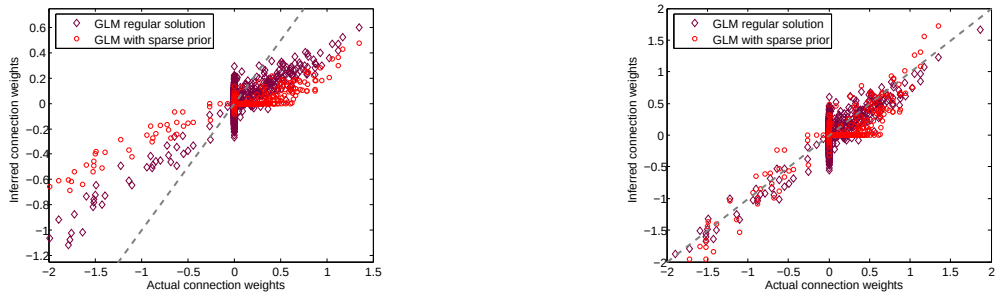

FIG. 4: A scatter plot of inferred connectivity weights vs. real connectivity weights using independent approximation and either GLM or sparse-prior GLM, for a network of $N = 50$ neurons imaged for $T = 800$ s with high SNR (40 Kph/neuron/frame, see Figure 5 below); $r^2 = 0.66$ for GLM solution and $r^2 = 0.85$ for sparse-prior GLM solution. Note that use of sparse prior allows to obtain significantly better approximation to the true connectivity matrix, although additional scaling bias is introduced in the estimate. Left panel is the original GLM solution with scaling-bias, and right panel is scaling-bias adjusted solution.

occurred independently, thus, allowing GLM explore full range of possible input configurations and disentangle potential common inputs. Estimation of the functional connectivity is fundamentally routed in observing changes in the spike rates conditioned on the state of the other neurons. Intuitively, such estimation can be compared to observing changes in $p(\mathbf{n}(t)) = \exp(\sum_j \omega_{ij} n_j(t))$ for different neural configurations $\mathbf{n}(t)$ or, equivalently, estimating vector $\mathbf{w}_i$ by observing a number of dot-products $\mathbf{w}_i\mathbf{n}(t)$ with different vectors $\mathbf{n}(t)$. Obviously, in order to be able to properly estimate all components of $\mathbf{w}_i$ the set of available $\mathbf{n}(t)$ should be rich enough to span all N dimensions of $\mathbf{w}_i$. In case of independent firing such condition of "full dimensionality" is clearly satisfied. Should this condition be violated, however, e.g. due to high correlation between spiking of few neurons, spike trains will not necessarily provide access to complete anatomical connectivity vector $\mathbf{w}_i$, and so the connection weights from the neurons providing correlated input may be "aggregated" into a single weight, split arbitrarily into a linear combination of weights, etc.

To test this effect we performed simulation of a hypothetical strongly coupled neural network, still with unstructured random sparse connectivity now consisting additionally of strong component. Strong connections component was chosen to dynamically build up the actual firing rate to ≈ 5 Hz from the base rate low $r = \exp(b_i) \approx 1$ Hz . Such strongly coupled network showed patterns of firing very different from weakly coupled networks considered above, Figure 11. In particular, large number of highly correlated, synchronously locked firings of many neurons were evident in this network. Likewise, GLM was not able to identify the true connectivity matrix correctly, Figure 11.

IV. DISCUSSION

Functional connectivity may fail to faithfully represent anatomical circuit structure if false correlations are present between different neurons, induced e.g. by common inputs, or if the dynamics of neural population is entirely concentrated on a low-dimensional subspace of the full configurational space $\mathbf{n}$. Note that these two statements are, in a sense, stating the same condition: if activity of different neurons is tightly correlated, their dynamics is concentrated on a low-dimensional plane and vice-versa - concentration of dynamics onto a low-dimensional plane

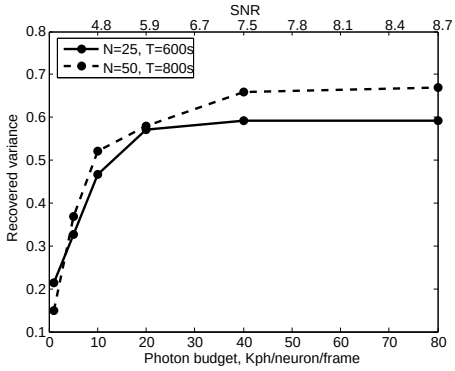

FIG. 5: Accuracy of inferred connectivity weights as function of noise amount in calcium imaging data, as measured by photon budget per neuron-frame and fluorescence signal to noise ratio SNR=$\left(E[\Delta F^2|\text{spk}]/E[\Delta F^2|\text{nospk}]\right)^{1/2}$, for networks of $N = 25$ and $N = 50$ neurons. Note that the photon counts on the order of 20-40 Kph/frame/neuron are required in order to achieve best reconstructions.

will be perceived as correlation in activity of different neurons. In turn, low dimensionality of the neural dynamics may be caused by different factors, including common input, small subset of command neurons driving the circuit, or even emergent property of a network. Low dimensionality of neural dynamics results in that the inference problem becomes underdetermined, i.e. there may exist directions in $\mathbf{w}_i$ along which connectivity is not constrained by neural activity data (i.e. directions orthogonal to the subspace of all observed neural activity configurations), or is poorly constrained. This, naturally, leads to $\mathbf{w}_i$ being poorly defined along these directions. The necessary condition for good correspondence between functional connectivity weights $\mathbf{w}_i$ and anatomical connectivity, therefore, is *full-dimensionality* of the observed set of neural configurations. In case of spontaneously firing system of neurons this condition is satisfied by many neuron-firings occurring independently, thus, allowing to fully sample all possible directions in $\mathbf{w}_i$. Still, spontaneously active preparation by itself may fail to display sufficient degree of independence between firing of neurons due to low-dimensionality of observed activity space, e.g. because of emergent properties of the circuit. In that case necessary variety of independent neural activity patterns may be enforced by randomly activating subsets of neurons via ChR2 or glutamate uncaging.

We also note that the correlations induced by secondary and so on synaptic transmissions (such as when neuron A results in firing of neuron B, which in turn results in firing by neuron C), are all properly resolved in GLM-fitting process via the so called explaining-away process. In other words, because we do not just identify correlations between neural firings with the functional connectivity weights ω_{ij}, but instead statistically fit a model of neural interactions, if found weights between neurons A and B, and B and C are sufficient to explain the correlation between A and C, the weight connecting A and C will not appear in the model - the correlation between A and C was "explained away" by correlations between A and B, and B and C. By this, the multi-synaptic firing patterns do not confuse our estimation process.

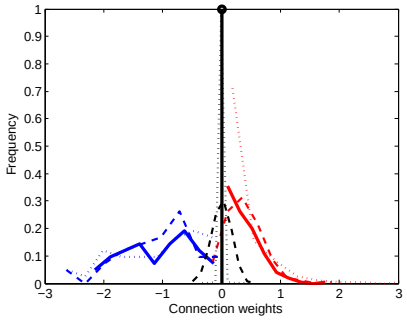

FIG. 6: Distribution of connectivity weights inferred using calcium imaging, for a network of $N = 50$ neurons and $T = 800$ s. The inferred distributions were rescaled to have the same mean with the true distributions, owing the time-discretization scaling bias discussed in the text. Left panel is for GLM solution, and right panel is for sparse-prior GLM solution. Blue curves are for inhibitory connections, red curves are for excitatory connections and black are for zero connections. Solid lines are original distributions and dashed lines are inferred distributions. In GLM solution the quality of the inferred weights is certainly sufficient to say whether a pairs of neurons is connected, or whether given neuron is inhibitory or excitatory with high reliability; and such statements may be made from sparse-prior GLM solution almost with certainty.

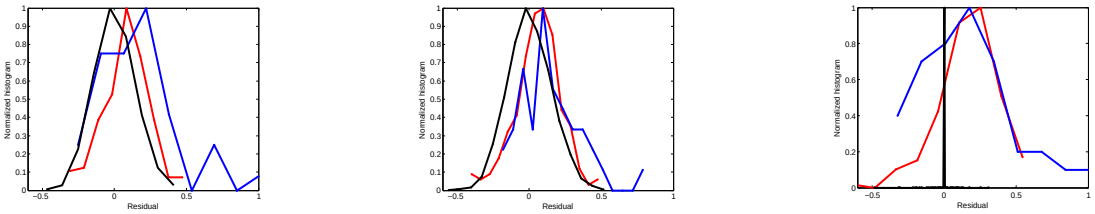

FIG. 7: Normalized histograms of residual errors in the inferred connectivity weights, for a network of $N = 50$ neurons and $T = 800$ s. The inferred distributions were rescaled to have the same mean with the true distributions, owing the time-discretization scaling bias discussed in the text. Left panel is for independent approximation using regular GLM, middle panel is for baseline regular GLM solution, and the right panel is for baseline sparse GLM solution.

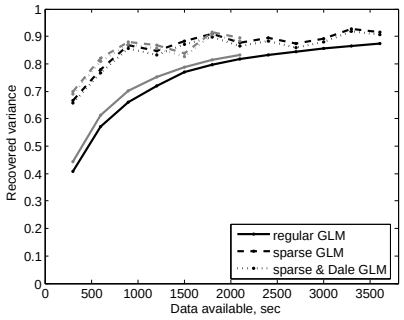

FIG. 8: Baseline accuracy of connectivity weights inference as the function of imaging time. Black lines are for $N = 50$ and gray lines are for $N = 100$. Note that accuracy does not depend on the number of neurons N, as shown in the Methods. Also, about 30 minutes of imaging time are sufficient for accurate estimation of the connectivity matrix using GLM solution, while the same accuracy of the reconstruction may be achieved with sparse-prior GLM solver already for 300-600 seconds of calcium imaging.

ADD SOME RAVINGS ABOUT PROPER/IMPROPER FUNCTIONAL CONNECTIVITY.

Acknowledgments

Thank everyone for their help and support [Bows, Bows, Bows] !!!

[1] C. Andrieu, A. Doucet, and A. Holenstein, *Particle markov chain monte carlo*, Working paper (2007).
[2] B. B. Averbeck and M. Seo, *The statistical neuronanatomy of frontal networks in the macaque*, PLOS Comp. Biol. **4** (2008), e1000050.
[3] J. Bohland, C. Wu, H. Barbas, B. Hermant, M. Bota, H. Breiter, H. Cline, J. Doyle, P. Freed, R. Greenspan, S. Haber, M. Hawrylycz, D. Herrera, C. Hilgetag, Z. Huang, A. Jones, E. Jones, H. Karten, D. Kleinfeld, R. Kotter, H. Lester, J. Lin, B. Mensh, S. Mikula, J. Panksepp, J. Price, J. Safdieh, C. Saper, N. Schiff, J. Schmahmann, B. Stillman, K. Svoboda, L. Swanson, A. Toga, D. Essen, J. Watson, and P. Mitra, *A proposal for a coordinated effort for the determination of brainwide neuroanatomical connectivity in model organisms at a mesoscopic scale*, arXiv (2009), 0901.4598.
[4] V. Braitenberg and A. Schuz, *Cortex: statistics and geometry of neuronal connectivity.*, Springer, Berlin, 1998.
[5] K. L. Briggman and W. Denk, *Towards neural circuit reconstruction with volume electron microscopy techniques.*, Current Opinions in Neurobiology **16** (2006), 562.
[6] B. M. Broome, V. Jayaraman, and G. Laurent, *Encoding and decoding of overlapping odor sequences*, Neuron **51** (2006), 467–482.
[7] E. J. Candes and J. Romberg, *Practical signal recovery from random projections.*, 2005.

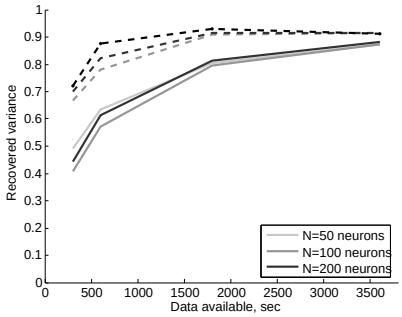

FIG. 9: Baseline accuracy of connectivity weights inference for for networks of different size from $N = 10$ to $N = 200$ neurons. Accuracy does not depend on the number of neurons N in agreement with theoretical analysis in Methods. 300-600 seconds of calcium imaging data are sufficient for estimating connectivity matrix using sparse-prior GLM solver, and about 30 minutes of observations are sufficient using GLM solver.

[8] S. H. Chalasani, N. Chronis, M. Tsunozaki, J. M. Gray, D. Ramot, M. B. Goodman, and C. I. Bargmann, *Dissecting a circuit for olfactory behaviour in caenorhabditis elegans*, Nature **450** (2007), 35.

[9] M. de Bono and Maricq A. V., *Neuronal substrates of complex behaviors in c. elegans*, Annu. Rev. Neurosci. **28** (2005), 451–501.

[10] D. Donoho and M. Elad, *Optimally sparse representation in general (nonorthogonal) dictionaries via L^1 minimization*, PNAS **100** (2003), 2197–2202.

[11] A. Doucet, N. de Freitas, and Gordon N., *Sequential monte carlo in practice*, Springer, 2001.

[12] N. A. Dunn, S. R. Lockery, J. T. Pierce-Shimomura, and J. S. Conery, *A neural network model of chemotaxis predicts functions of synaptic connections in the nematode caenorhabditis elegans.*, Journal of Computational Neuroscience **17** (2004), 137–47.

[13] P. Fearnhead and P. Clifford, *On-line inference for hidden markov models with particle filters*, J. R. Statist. Soc. B **65** (2003), 887–99.

[14] A. E. Gelfand and A. F. M. Smith, *Sampling-based approaches to calculating marginal densities*, Journal of the American Stat. Assoc. **85** (1990), 398–409.

[15] Werner Gobel and Fritjof Helmchen, *In vivo calcium imaging of neural network function*, Physiology **22** (2007), no. 6, 358–365.

[16] S. M. Gomez-Urquijo, C. Reblet, J. L. Bueno-Lopez, and I. Gutierrez-Ibarluzea, *Gabaergic neurons in the rabbit visual cortex: percentage, distribution and cortical projections*, Brain Res **862** (2000), 171–9.

[17] J. M. Gray, J. J. Hill, and C. I. Bargmann, *A circuit for navigation in caenorhabditis elegans.*, PNAS **102** (2005), 3184.

[18] P. Hagmann, L. Cammoun, X. Gigandet, R. Meuli, C. Honey, V. Wedeen, and O. Sporns, *Mapping the structural core of human cerebral cortex*, PLoS Biology **6** (2008), no. 7, e159.

[19] P. Hagmann, M. Kurant, X. Gigandet, P. Thiran, V. Wedeen, R. Meuli, and J.-P. Thiran, *Mapping human whole-brain structural networks with diffusion mri*, PLoS ONE **2** (2007), no. 7, e597.

[20] M. Helmstaedter, K. L. Briggman, and W. Denk, *3d structural imaging of the brain with photons and electrons.*, Current Opinions in Neurobiology (2009), Epub.

[21] Y. Ikegaya, M. Le Bon-Jego, and R. Yuste, *Large-scale imaging of cortical network activity with calcium indicators.*,

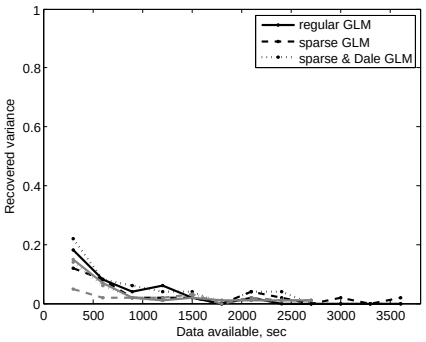

FIG. 10: Baseline accuracy of the inferred neuron type (excitatory or inhibitory) as the function of imaging time. Black lines are for $N = 50$ and gray lines are for $N = 100$. Better than 95% accuracy is achieved in identification of neuron type.

Neuroscience Research **52** (2005), 132–8.

[22] V. Jain, J. Murray, F. Roth, S. Turaga, V. Zhigulin, K. Briggman, M. Helmstaedter, W. Denk, and H. Seung, *Supervised learning of image restoration with convolutional networks.*, 2007, pp. 1–8.

[23] L. M. Jones, A. Fontanini, B. F. Sadacca, P. Miller, and D. B. Katz, *Natural stimuli evoke dynamic sequences of states in cortical ensembles*, Proceedings of the National Academy of SciencesJournal of Neuroscience **104** (2007), 18772–7.

[24] E. Jurrus, T. Tasdizen, P. Koshevoy, P. Fletcher, M. Hardy, C. Chien, W. Denk, and R. Whitaker, *Axon tracking in serial block-free scanning electron microscopy.*, 2006.

[25] S. Koyama and L. Paninski, *Efficient computation of the maximum a posteriori path and parameter estimation in integrate-and-fire and more general state-space models*, Journal of Computational Neuroscience **In press** (2009).

[26] S. Lefort, C. Tomm, J.-C. Floyd Sarria, and C. C. H. Petersen, *The excitatory neuronal network of the c2 barrel column in mouse primary somatosensory cortex*, Neuron **61** (2009), 301–16.

[27] A. Litke, N. Bezayiff, E.J. Chichilnisky, W. Cunningham, W. Dabrowski, A. Grillo, M. Grivich, P. Grybos, P. Hottowy, S. Kachiguine, R. Kalmar, K. Mathieson, D. Petrusca, M. Rahman, and A. Sher, *What does the eye tell the brain? development of a system for the large scale recording of retinal output activity*, IEEE Trans Nucl Sci (2004), 1434–1440.

[28] A. M. Litke, E. J. Chichilnisky, W. Dabrowski, A. A. Grillo, P. Grybos, S. Kachiguine, M. Rahman, and G. Taylor, *Large-scale imaging of retinal output activity*, Nucl. Instrum. Methods A **501** (2003), 298–307.

[29] M. Meister, J. Pine, and D. A. Baylor, *Multi-neuronal signals from the retina: acquisition and analysis*, J. Neuroscie. Methods **51** (1994), 95–106.

[30] T. Minka, *A family of algorithms for approximate Bayesian inference*, Ph.D. thesis, MIT, 2001.

[31] Y. Mishchenko, *Automation of 3d reconstruction of neural tissue from large volume of conventional serial section transmission electron micrographs.*, Journal of Neuroscience Methods **176** (2009), 276–289.

[32] ———, *Detecting, quantifying and classifying synapses using light microscopy for reconstruction of neural circuits*, Preprint (2009).

[33] ———, *Strategies for identifying exact structure of neural circuits with broad light microscopy connectivity probes*, Preprint: http://precedings.nature.com/documents/2669/version/2 (2009).

[34] S. Nagayama, S. Zheng, W. Xiong, L. V. Fletcher, A. V. Masurkar, D. J. Davis, V. A. Pieribone, and W. R. Chen, *In vivo simultaneous tracing and ca^{2+} imaging of local neuronal circuits.*, Neuron **53** (2007), 789–803.

[35] R. Neal, M. Beal, and S. Roweis, *Inferring state sequences for non-linear systems with embedded hidden Markov models*,

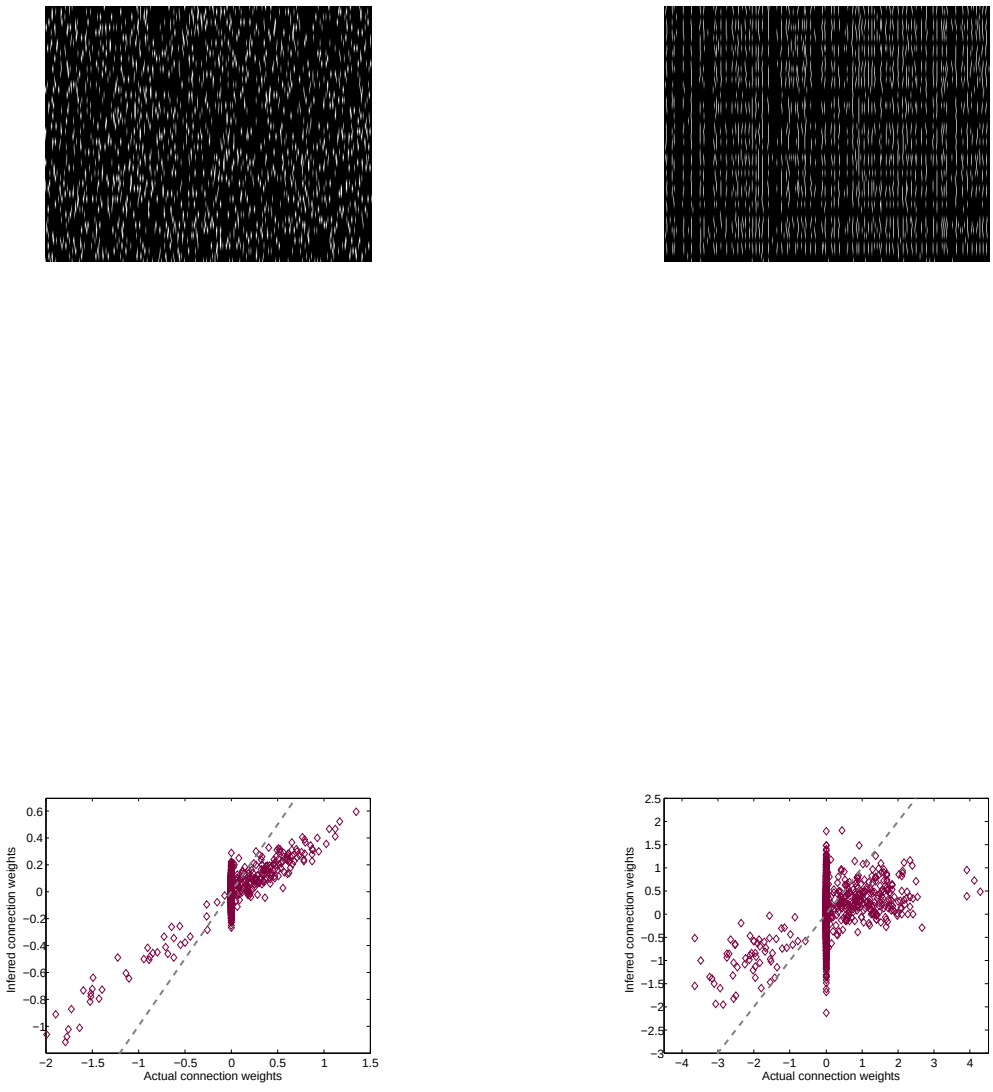

FIG. 11: 15 sec of simulated spike trains for a weakly coupled (upper-left) and strongly coupled (upper-right) stochastic networks. Note that in weakly coupled network spikes are sufficiently uncorrelated to allow access to all different neural connectivity configurations necessary to estimate complete anatomical connectivity vectors $\mathbf{w}_i$. In strongly coupled case many instances of highly synchronous locked firings are evident, thus reducing dimensionality of the observed dynamic space of the network, and preventing functional connectivity from faithfully representing anatomical connectivity. Accordingly, GLM solution for strongly coupled neural network (lower-right) does not provide access to the structure of anatomical connectivity as opposed to weakly-coupled case (lower-left).

NIPS **16** (2003).
[36] T. Nevian and F. Helmchen, *Calcium indicator loading of neurons using single-cell electroporation*, Pflugers Archiv Eur. J. Nerosci. **454(4)** (2007), 675–88.
[37] M. Okatan, M. Wilson, and E. Brown, *Analyzing functional connectivity using a network likelihood model of ensemble neural spiking activity*, Neural Computation **17** (2005), 1927–1961.
[38] L. Paninski, M. Fellows, S. Shoham, N. Hatsopoulos, and J. Donoghue, *Superlinear population encoding of dynamic hand trajectory in primary motor cortex*, J. Neurosci. **24** (2004), 8551–8561.
[39] J. Pillow and P. Latham, *Neural characterization in partially observed populations of spiking neurons*, NIPS (2007).
[40] J. Pillow, J. Shlens, L. Paninski, A. Sher, A. Litke, E.J. Chichilnisky, and E. Simoncelli, *Spatiotemporal correlations and visual signaling in a complete neuronal population*, Nature **454** (2008), 995–999.
[41] L. Rabiner, *A tutorial on hidden Markov models and selected applications in speech recognition*, Proceedings of the IEEE **77** (1989), 257–286.
[42] M. I. Rabinovich, R. Huerta, P. Varona, and V. S. Afraimovich, *Transient cognitive dynamics, metastability, and decision making*, PLoS Computational Biology **4** (2008), no. 5, e1000072.
[43] F. Rigat, M. de Gunst, and J. van Pelt, *Bayesian modelling and analysis of spatio-temporal neuronal networks*, Bayesian Analysis **1** (2006), 733–764.
[44] R. J. Sayer, M. J. Friedlander, and S. J. Redman, *The time course and amplitude of epsps evoked at synapses between pairs of ca3/ca1 neurons in the hippocampal slice*, J. Neurosci. **10** (1990), 826–36.
[45] R. Shumway and D. Stoffer, *Time series analysis and its applications*, Springer, 2006.
[46] S. Song, P. J. Sjostrom, M. Reiql, S. Nelson, and D. B. Chklovskii, *Highly nonrandom features of synaptic connectivity in local cortical circuits.*, PLoS Biology **3** (2005), e68.
[47] I. H. Stevenson, J. M. Rebesco, N. G. Hatsopoulos, Z. Haga, L. E. Miller, and K. P. Kording, *Bayesian inference of functional connectivity and network structure from spikes*, IEEE Trans. Neural Systems and Rehab. **17** (2009), 203–13.
[48] I. H. Stevenson, J. M. Rebesco, L. E. Miller, and K. P. Kording, *Inferring functional connections between neurons*, Curr. Opin. Neurobiol. **18** (2008), 582–8.
[49] J. T. Vogelstein, B. O. Watson, A. M. Packer, R. Yuste, B. Jedynak, and L. Paninski, *Spike inference from calcium imaging using sequential monte carlo methods*, Preprint (2009).
[50] W. W. Denk and H. Horstmann, *Serial block-face scanning electron microscopy to reconstruct three-dimensional tissue nanostructure*, PLOS Biol. **2** (2004), e329.
[51] J. White, E. Southgate, J. N. Thomson, and S. Brenner, *The structure of the nervous system of the nematode caenorhabditis elegans.*, Philosophical Transactions of Royal Society London. Series B, Biological Sciences **314** (1986), no. 1165, 1–340.
[52] wormatlas.org, *Wormatlas: a database of behavioral and structural anatomy of caenorhabditis elegans.*
[53] W. Wu, J. Kulkarni, N. Hatsopoulos, and L. Paninski, *Neural decoding of goal-directed movements using a linear statespace model with hidden states*, Computational and Systems Neuroscience Meeting (2008).
[54] R. Yasuda, E. A. Nimchinsky, V. Scheuss, T. A. Pologruto, T. G. Oertner, B. L. Sabatini, and K. Svoboda, *Imaging calcium concentration dynamics in small neuronal compartments*, Sci STKE **219** (2004), p15.